Journal of Materials Chemistry B

PAPER

View Article Online
View Journal | View Issue



Cite this: J. Mater. Chem. B, 2016, 4, 7974

# Effects of magnesium silicate on the mechanical properties, biocompatibility, bioactivity, degradability, and osteogenesis of poly(butylene succinate)-based composite scaffolds for bone repair

Zhaoying Wu,[a] Kai Zheng,[b] Jue Zhang,[a] Tingting Tang,[c] Han Guo,[d] Aldo. R. Boccaccini*[b] and Jie Wei*[a]

Received 18th September 2016,
Accepted 3rd November 2016

DOI: 10.1039/c6tb02429g

www.rsc.org/MaterialsB

Bioactive scaffolds of magnesium silicate (m-MS)/poly(butylene succinate) (PBSu) composites were fabricated by a solvent casting–particulate leaching method for bone regeneration. The scaffolds had a hierarchical porous structure with interconnected macropores (300–500 μm), micropores (1–10 μm) and mesopores (~5 nm). In addition, the composite scaffolds were degradable in Tris-HCl solution and formed apatite on their surfaces in simulated body fluid, indicating good degradability and bioactivity *in vitro*. Compared with PBSu scaffolds, the composite scaffolds improved the *in vitro* attachment, proliferation and osteogenic differentiation of MC3T3-E1 cells, revealing good cytocompatibility. Furthermore, the model of rabbit femur cavity defects was used to evaluate the *in vivo* osteogenesis of the composite scaffolds. The results of synchrotron radiation-based mCT (SRmCT) imaging, histological analysis and immunohistochemistry showed that the composite scaffolds were gradually degraded and replaced by new bone, and the scaffolds with 40 wt% m-MS (C40) almost completely disappeared after 12 weeks of implantation, indicating that the scaffolds containing m-MS enhanced new bone formation. The results demonstrated that the bioactive m-MS/PBSu composite scaffolds with good biocompatibility, degradability, bioactivity and osteogenesis are promising biomaterials for bone repair.

## 1. Introduction

In recent years, biodegradable polymeric materials have been widely used to assemble bone tissue engineering scaffolds with 3D structures.[1] Poly(α-hydroxy acids), including poly(lactic acid) and poly(glycolic acid),[2,3] are extensively used for biomedical applications and have already been approved by the U.S. Food and Drug Administration (FDA). Although poly(α-hydroxy acids) have been widely used in clinical practice, their acidic degradation by-products could trigger strong inflammatory responses.[4] Poly(butylene succinate) (PBSu), a biodegradable aliphatic polyester, is an ideal alternative to poly(α-hydroxy acids) because of its excellent biocompatibility, good processing ability, as well as non-toxic degradation products.[5] However, PBSu also has some disadvantages that may narrow its biomedical applications. For example, PBSu is a hydrophobic material, which can affect cell attachment and the infiltration of the cell into a porous structure, has a slow degradation rate and biological inertness, which may hinder the integration of PBSu into host bone tissue and osteogenesis.[6]

Based on the above rationale, much effort (such as copolymerization, blending and compositing) has been made to modify PBSu.[7] On account of its excellent mechanical properties and good biodegradability, various reports suggested the use of PBSu-based random or block copolymers as green materials.[8] Blending PBSu with poly(lactic acid) (PLA), poly(hydroxybutyrate) (PHB) or natural polymers, such as chitosan and silk fiber, has also been widely investigated.[9,10] Furthermore, the use of inorganic fillers is still the main approach for the modification of polymeric materials.[11]

[a] Key Laboratory for Ultrafine Materials of Ministry of Education, East China University of Science and Technology, Shanghai 200237, P. R. China. E-mail: jiewei7860@sina.com; Fax: +86-021-64251358; Tel: +86-021-64251308
[b] Institute of Biomaterials, Department of Materials Science and Engineering, University of Erlangen-Nuremberg, Cauerstrasse 6, 91058 Erlangen, Germany. E-mail: aldo.boccaccini@ww.uni-erlangen.de; Fax: +49-91318528602; Tel: +49-91318528601
[c] Shanghai Key Laboratory of Orthopaedic Implants, Department of Orthopaedic Surgery, Shanghai Ninth People's Hospital, Shanghai Jiaotong University, School of Medicine, Shanghai 200011, P. R. China
[d] Shanghai Synchrotron Radiation Facility, Shanghai Institute of Applied Physics, Chinese Academy of Sciences, Shanghai 201800, P. R. China

In the previous investigation, mesoporous magnesium silicate (m-MS) has been revealed to possess rapid degradability, excellent *in vitro* bioactivity and cytocompatibility.[12] Some researchers have confirmed that the incorporation of bioactive metal elements (such as Mg, Sr and Zn *etc.*) into amorphous silica walls exhibited stimulation effects on osteoblast differentiation and therefore the formation of new bone *in vivo*.[13,14] Furthermore, the incorporation of Mg-containing particles into scaffolds could tailor a number of important properties, such as crystallinity and degradation, to satisfy the requirements for bone tissue engineering.[15] It is therefore expected that incorporation of m-MS into PBSu scaffolds could modify its properties and overcome the above limitations of using PBSu scaffolds alone for bone regeneration.

In the present study, m-MS/PBSu composite scaffolds with a hierarchical macro–micro-mesoporous structure were fabricated using a solvent casting–salt leaching method. The effects of m-MS incorporation on the pore structure, hydrophilicity, bioactivity and *in vitro* degradability of the composite scaffolds were studied. Moreover, the attachment, proliferation and osteogenic differentiation of MC3T3-E1 cells on the scaffolds were evaluated. By using the model of rabbit femur cavity defects, the osteogenesis and degradability of scaffolds *in vivo* were evaluated by using SRmCT imaging, histology and immunohistochemistry.

## 2. Experimental

### 2.1 Preparation and characterization of m-MS/PBSu composite scaffolds

m-MS/PBSu composite scaffolds were prepared by a solvent casting–particulate leaching method.[16] Briefly, PBSu particles (Shanghai Showa Highpolymer Co. Ltd) were dissolved in selected volumes of dimethyl formamide (Shanghai Lingfeng Chemical Reagent Co. Ltd) to prepare a polymer solution. Selected amounts of m-MS were added to PBSu solution with continuous stirring to obtain a uniform dispersion. Sodium chloride (NaCl) particulates ranging in diameter from 300 to 500 μm were added to the m-MS/PBSu composite slurry at the weight ratio of 8 : 1 and the mixture was stirred for 10 min. The mixture was casted into moulds to form three-dimensional (3D) scaffolds. The moulds with the mixture were air-dried under a ventilation hood overnight to remove the solvent by evaporation. After evaporation, the salt particulates were leached out by immersing the scaffolds into deionized (DI) water for 48 h, with the refreshment of water every 8 h. The scaffolds were air-dried for 24 h and vacuum-dried for 12 h.

The m-MS/PBSu composite scaffolds containing 20 wt% and 40 wt% m-MS were prepared and labelled C20 and C40 accordingly. Pure PBSu scaffolds were prepared as a control (C0).

The phase composition and crystallinities of m-MS/PBSu composite scaffolds were characterized by X-ray diffraction (XRD; Geigerflex, Rigaku Co. Ltd, Japan), and crystallinity was calculated from the area ratio of crystalline peaks to amorphous halo in the X-ray diffraction patterns. Fourier transform infrared spectrometry (FTIR, Magna-IR 550, Nicolet) was conducted to analyse the structural characteristics of the scaffolds, while the porous structure and surface morphology were observed by scanning electron microscopy (SEM; S-3400N, Hitachi, Japan). Additionally, synchrotron radiation-based micro-computed tomography (SRmCT) was carried out to understand the porous structure of the scaffolds.

### 2.2 Compressive strength, porosity and water absorption

The compressive strengths of scaffolds were determined using a mechanical testing machine (HY-0230, Shanghai, China) at room temperature. Cylindrical scaffolds ($\Phi$ 6 × 6 mm) were loaded with a 1 kN cell load at the speed of 1 mm min$^{-1}$ until crush. The compressive strengths were determined from the peak of the stress–strain curve.

The porosity of the scaffolds was determined by using the Archimedes method at room temperature,[17] which was calculated as:

$$\text{Porosity (\%)} = (m_2 - m_1)/(m_2 - m_3) \times 100\%$$

where $m_1$, $m_2$ and $m_3$ are the dry weight of the scaffolds, the wet weight of the scaffolds (including water) and the weight of the scaffolds suspended in water (subtracting buoyancy from $m_1$), respectively.

To evaluate the water absorption, the scaffolds with the size of $\Phi$ 12 × 2 mm were weighed ($W_0$) and subsequently immersed in DI water for 48 hours at 37 °C and 100 rpm in a water bath. The weight of the scaffolds ($W_t$) after being removed from DI water was determined immediately after wiping off the leftover water on the surface. The water absorption ratio was calculated by[12]

$$\text{Water absorption ratio (\%)} = (W_t - W_0)/(W_0) \times 100\%$$

### 2.3 *In vitro* degradability

To assess the *in vitro* degradation behaviours of the scaffolds, C0, C20 and C40 with the size of $\Phi$ 12 × 2 mm were weighed ($W_0$) before immersion in Tris-HCl solution (0.01 M, pH 7.4). The experiment was conducted at 37 °C and a constant shaking speed of 60 rpm min$^{-1}$ in an orbital shaker for 84 days. At target intervals, the scaffolds were taken out, rinsed gently with DI water, dried at 37 °C until exhaustion and weighed ($W_i$). The weight loss was calculated according to the following equation:[18]

$$\text{Weight loss (\%)} = (W_0 - W_i)/(W_0) \times 100\%$$

where $W_0$ is the initial dry weight and $W_i$ is the dry weight at time $i$.

The pH variation of the solution during the whole period was monitored by using a pH meter (FE20, Mettler Toledo).

### 2.4 *In vitro* bioactivity

The assessment of *in vitro* bioactivity was tested by immersing the samples in simulated body fluid (SBF, pH 7.4) at a ratio of 1 mg mL$^{-1}$ for different time periods. At each pre-determined time point (6, 12, 24, 72, and 120 hours), the scaffolds were withdrawn, rinsed with DI water and air-dried at room temperature overnight. The surface morphology and phase composition of the scaffold were evaluated by SEM and energy dispersive spectroscopy

(EDS, Falcon, USA), respectively. The changes in the ion concentrations of Ca, P, Mg and Si in SBF after sample soaking for different time periods were determined by inductively coupled plasma-atomic emission spectroscopy (ICP-AES; IRIS 1000, Thermo Elemental, USA).

### 2.5 Cell culture

All scaffolds ($\Phi$ 12 × 2 mm) were sterilized by ethylene oxide for 4 hours before being sealed in a sterile centrifuge tube for subsequent cell experiments. Mouse pre-osteoblastic cell lines (MC3T3-E1) were cultured in Dulbecco's Modified Eagle Medium (DMEM; Thermo Fisher Scientific Inc., USA) supplemented with 10% fetal bovine serum (FBS; GibcoBRL, Grand Island, NY, USA), 1% penicillin (100 U $mL^{-1}$) and streptomycin sulphate (100 mg $mL^{-1}$) (Gibco BRL, USA). The cells were cultured in a humidified atmosphere at 37 °C and 5% $CO_2$. The culture medium was replaced every 3 days.

**2.5.1 Cell viability.** The 1 mL culture medium with 3 × $10^4$ cells were seeded on each scaffold placed in a 24-well plate. Standard culture medium with only cells was used as a control. The cell viability was assessed by the cell counting kit-8 (CCK-8; Dojindo Molecular Technologies Inc., Japan) assay after 3, 6 and 12 hours of culture using a standard procedure.[19] Briefly, at the pre-determined time points, the scaffolds were rinsed with sterile phosphate-buffered saline (PBS, pH = 7.4) three times and then transferred to a brand new 24-well plate to avoid the effects of cells attached on the used 24-well plate. 500 μL of the mixture solution containing DMEM and CCK-8 solution (10 : 1, v : v) were added to each well and empty wells containing DMEM without scaffolds were set up as a blank control. After being incubated for 3 hours, the supernatant was removed and characterized by a microplate reader (Synergy HT, Bio-tek, Winooski, Vermont, USA) at 450 nm to get optical density (OD) values. The OD of blank control was subtracted from the obtained ODs of the test groups.

The viability of MC3T3-E1 cells on the scaffolds after culturing for 12 hours was also determined using a live/dead assay kit (Abcam, Inc., Cambridge, UK) according to the manufacturer's protocol. In brief, the cells were gently washed with sterile PBS, then incubated with standard working reagents for 25 min at 37 °C and finally observed by confocal laser scanning microscopy (CLSM; Nikon A1R, Japan).

**2.5.2 Cell proliferation.** The cell proliferation was determined by the CCK-8 assay at day 1, 3, and 5. The procedure was similar to that of the cell viability test, but the seeding density of cells was 5 × $10^3$ cells per well. Briefly, the scaffolds were transferred to a new 24-well plate and then incubated with CCK-8 solution for 3 hours at each target interval. Then, the supernatant was read using a microplate reader at 450 nm to obtain the ODs and modified ODs. The cell proliferation was expressed as relative proliferation rates, in which the modified ODs at day 3 and 5 were normalized to those at day 1 for each group.[20]

**2.5.3 Cell morphology.** Cell morphology was visualized by detecting the filamentous actin of the cytoskeleton of MC3T3-E1 cells into scaffolds. The scaffolds were washed gently twice with PBS solution to remove the unattached cells after incubation for 3 days. Then the cells on specimens were fixed with 2.5% glutaraldehyde for 3 hours and subsequently permeabilized with 0.1% Triton X-100 in PBS solution for 10 min. After being washed three times with PBS solution, the cells were stained with 4,6-diamidino-2-phenylindole dihydrochloride (DAPI, Sigma) and fluorescein isothiocyanate (FITC, Sigma). The cell morphology and spreading were finally observed by CLSM.

**2.5.4 Alkaline phosphatase (ALP) activity.** MC3T3-E1 cells with a density of 4 × $10^4$ cells $mL^{-1}$ were used to evaluate the effect of the scaffolds on osteogenic differentiation. After incubation in a 24-well plate for 24 h, the culture medium was changed to the osteogenic induction medium: the DMEM was supplemented with 10% FBS, 0.1 μM dexamethasone (Sigma), 50 μM ascorbic acid (Sigma), and 10 μM β-glycerophosphate sodium (Sigma). These media were renewed every 2 days for 2 weeks. After 7, 10 and 14 days of culture with the above osteogenic induction medium in a 24-well plate, the substrates were washed three times with PBS solution, and then lysed in a 0.2% TritonX-100 solution through four standard freeze–thaw cycles. The ALP activity was determined according to the procedures as mentioned in previous article, with the tissue culture plate (TCP) as a control.[12]

**2.5.5 Ion concentrations in cell culture medium.** At selected time points (1, 3, 5, 7, 10 and 14 days), the cell culture medium was collected and centrifuged for 20 min at 1500 rpm. The supernatants were mixed with nitric acid ($HNO_3$, 0.3 mol $L^{-1}$) at a ratio of 1 : 2 (v : v) and the ion concentrations of Mg and Si were measured by ICP-AES. The medium for MC3T3-E1 cell culture without scaffolds served as the negative control.

### 2.6 Implantation *in vivo*

**2.6.1 Animal surgical procedures.** The effects of scaffolds on bone formation *in vivo* were evaluated using the model of rabbit femur cavity defects. All animal procedures were performed in compliance with the relevant laws and institutional guidelines, and were approved by the Institutional Animal Care and Use Committee of National Tissue Engineering Research Center of China (Shanghai, China).[21] The National Institutes of Health guidelines for the care and use of laboratory animals (NIH Publication No. 85–23 Rev. 1985) were observed. New Zealand white rabbits (5 months old), weighting on average 3 kg were randomly assigned to three groups corresponding to C0, C20 and C40 scaffolds. Each group was composed of 9 rabbits and 3 experimental animals were assigned for each scheduled time (4, 8 and 12 weeks). After being anesthetized by intramuscular injection using Zoletil 50 at 25 mg $kg^{-1}$ and 2% Rompon at 0.15 mL $kg^{-1}$, the defects (6 mm in diameter and 6 mm in depth) were created in the left shaved knee with a medium speed burr, and the scaffolds (C0, C20 and C40) were implanted into the defects. At 4, 8 and 12 weeks post-implantation, the rabbits were sacrificed successfully by an overdose of pentobarbital and the femurs were removed to obtain animal experimental samples fixed in 10% phosphate-buffered formalin.

**2.6.2 SRmCT images of implanted scaffolds.** In order to evaluate the bone repair effects of different implanted scaffolds *in vivo*, the new bone formation in harvested bone specimens was observed and imaged with SRmCT at beamline BL13W of

 

SSRF (Shanghai, China). The X-ray source settings were 30 keV with a sample-to-detector distance of 1.6 m, in which a VHR detector with a pixel size set to 9 mm was used to record images. The 2D images were redigitized with an 8-bit data format. The 3D scaffolds implanted in bone defects were finally reconstructed and visualized using VG Studio MAX 2.0 software (Volume Graphics, Heidelberg, Germany).

**2.6.3 Histological analysis and immunohistochemistry.** After SRmCT scanning, the harvested bony samples were assigned to histological analysis. Briefly, the extracted bones were fixed in 10% phosphate-buffered formalin, decalcified with 12.5% ethylene diamine tetra-acetic acid (EDTA), embedded in paraffin wax in turn, and finally cut into 4 mm-thick sections using a microtome. The sections were stained by hematoxylin/eosin (H&E) and Masson trichrome staining, respectively, before being observed microscopically (TE2000U, Nikon, Japan). Three microscopy images were obtained from three randomly selected areas for each sample and then histomorphometrically evaluated using Image-Pro Plus. The number of pixels labeled by H&E in image was determined as percentages of the newly formed bone area. Quantitative analysis was performed for Masson trichrome staining using Image-ProPlus to determine the ratios of mature bone, new bone and residual materials.

Immunohistochemistry was used to investigate the new bone tissue formation after the implantation of scaffolds *in vivo*. Briefly, the sections were dewaxed and incubated with primary antibodies against BMP-2 (Bone Morphogenetic Protein, 1:25 dilution; Abcam, Inc., Cambridge, UK) to recognize osteogenesis. A biotinylated antirabbit antibody (Boster Co. Ltd, Shanghai, China) was used as a secondary antibody, and the sections were stained using the avidin–biotin complex method (ABC, Vector Laboratories, Inc., Peterborough, UK) with a DAB substrate (DAKO, Cambridge, UK) for staining the slides. Finally, the sections were counterstained with hematoxylin, mounted and then observed with a light microscope. Quantitative analysis was performed using Image-Pro Plus to determine the positive expression ratios after the implantation of scaffolds for 4, 8, and 12 weeks.

### 2.7 Statistical analysis

All quantitative data were expressed as mean ± standard deviation (M ± SD). Five samples were used in cell biology experiments, while three samples were used for other tests. Statistical significance was carried out using one-way analysis of variance (ANOVA) with Tukey's *post hoc* test, where $P < 0.05$ was considered to be statistically significant. The notation "*" denotes $P < 0.05$ and "**" denotes $P < 0.01$.

## 3. Results

### 3.1 Characterization of scaffolds

The XRD patterns of m-MS, C0, C20 and C40 scaffolds are presented in Fig. 1A. The diffraction peaks at 19.3°, 22.2°, 25.9° and 29° could be found in C0, which is in accordance with the crystallographic phases of PBSu of (002), (110), (121) and (111), respectively.[22] A broad reflection at $2\theta = 15$–35° was exhibited in the XRD pattern of m-MS, indicating the typical amorphous silicate structure of m-MS. The position of the diffraction peaks for PBSu in C20 and C40 was not altered after the introduction of m-MS as compared with C0. Moreover, it is found that the intensity of the peaks of PBSu in the composite scaffolds slightly decreased due to the decrease of the crystallinity as compared with PBSu. As shown in Table 1, the crystallinity values of C0, C20 and C40 were 57.2, 49.4 and 35.8%, respectively.

Fig. 1B illustrates the FTIR spectra of m-MS, C0, C20 and C40 scaffolds. The characteristic band of PBSu appeared at 1730 $cm^{-1}$, corresponding to the C═O stretching. The characteristic bands of m-MS appeared at 1082, 799 and 457 $cm^{-1}$, corresponding to the Si–O–Si asymmetric stretching, symmetric stretching and bending. Besides, the peaks at 1640 and 3450 $cm^{-1}$ were ascribed to the H–OH bending vibrations and the free O–H groups of adsorbed water molecules, respectively. Interestingly, the peak at 3450 $cm^{-1}$ appeared in both C20 and C40, while a weak peak at 1640 $cm^{-1}$ appeared only in C40. In other words,

Table 1 Porosity, water absorption, compressive strength and crystallinity of the scaffolds

| Scaffolds | Porosity (%) | Water absorption (%) | Compressive strength (MPa) | Crystallinity (%) |
|---|---|---|---|---|
| C0 | 64.5 ± 1.9 | 274.6 ± 6.8 | 2.2 ± 0.8 | 57.2 |
| C20 | 67.3 ± 2.6 | 381.1 ± 24.5 | 3.0 ± 1.2 | 49.4 |
| C40 | 69.7 ± 3.2 | 420.9 ± 29.3 | 4.1 ± 1.9 | 35.8 |

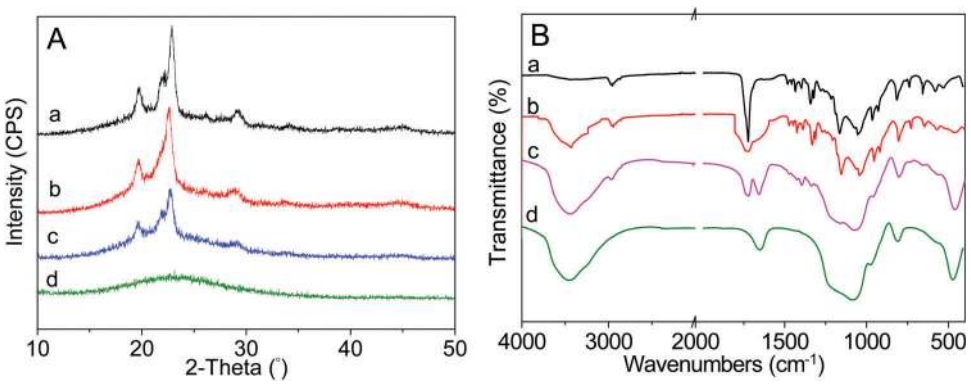


Fig. 1 XRD (A) and FTIR (B) of C0 (a), C20 (b), and C40 (c) scaffolds, and m-MS (d).

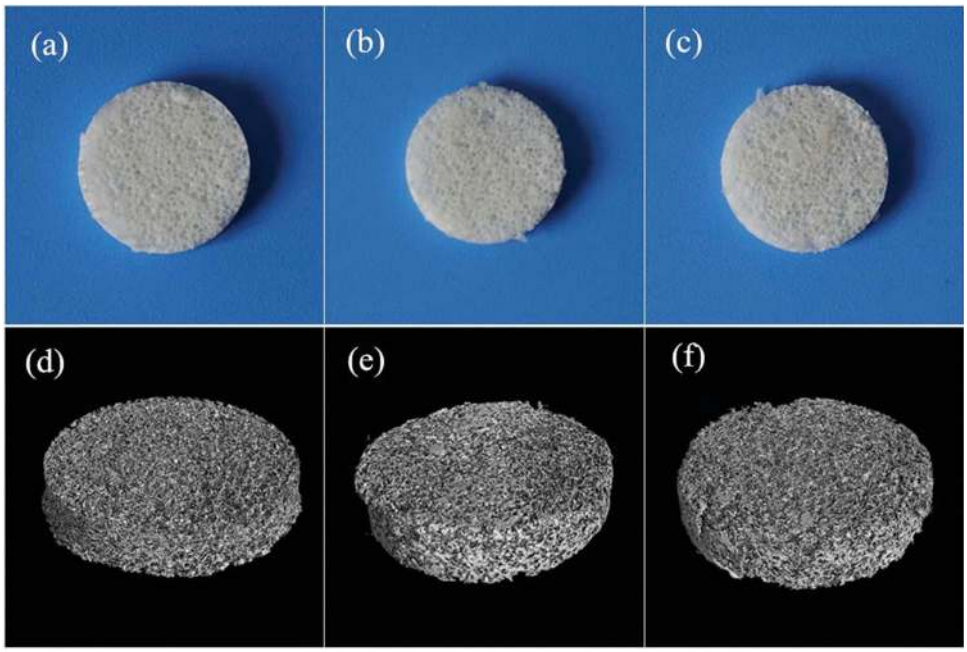


Fig. 2 Digital photos (a–c) and SRmCT (d–f) of C0 (a and d), C20 (b and e) and C40 (c and f) scaffolds ($\Phi$ 12 × 2 mm).

the spectra of C20 and C40 scaffolds exhibited the characteristic bands of both PBSu and m-MS, confirming the incorporation of m-MS into PBSu.

Fig. 2 shows the digital photographs and representative 3D images of C0, C20 and C40 scaffolds reconstructed by SRmCT, respectively. All the scaffolds showed a reticular structure without an obvious visual difference in macroscopic size (Fig. 2a–c). More importantly, it is found that the three-dimensional scaffolds had interconnected macropores and exhibited a highly uniform porous structure (Fig. 2d–f).

The SEM images of the scaffolds are shown in Fig. 3. It is found that the pore size of these scaffolds (C0, C20 and C40) was about 400 μm, which was consistent with the size of the NaCl particles used to prepare the scaffolds. The results also indicated that no obvious difference in the pore size of the scaffolds after introduction of m-MS was observed. In the high magnification SEM micrographs, it is found that the C0 scaffolds showed a relatively smooth surface with pores (Fig. 3d) while the C20 (Fig. 3e) and C40 (Fig. 3f) scaffolds showed a rougher porous surface.

The average porosity of the C0 scaffolds was around 64.5% (Table 1) while the C20 and C40 scaffolds had the porosity values of 67.3% and 69.7%, respectively, indicating that the introduction of m-MS did not lead to a significant influence on the porosity of the scaffolds.

Table 1 shows the water absorption and compressive strength of C0, C20 and C40 scaffolds. Increasing the m-MS content in the scaffolds (C20 and C40), the water absorption

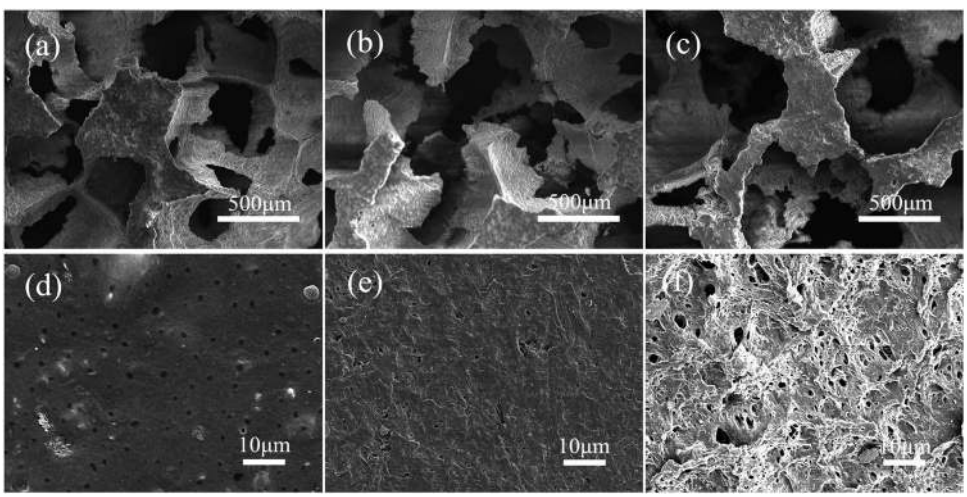


Fig. 3 Surface morphology of C0 (a and d), C20 (b and e) and C40 (c and f) scaffolds observed using SEM images.

 

significantly increased from 274.6% (C0) to 381.1% and 420.9%, respectively. In addition, the compressive strength of the scaffolds increased from 2.2 MPa to 4.1 MPa with an increase in the m-MS content from 0 to 40 wt%. The results revealed that the addition of m-MS to PBSu contributed to the improvement of water absorption and compressive strength.

### 3.2 *In vitro* degradability of scaffolds

The weight loss percentage ratio (Fig. 4A) was used to express the degradation behavior of the specimens in the course of soaking in Tris-HCl buffer solution. It is found that the weight loss of all the scaffolds increased as a function of soaking time. The weight loss ratio increased with the increase of m-MS content in composite scaffolds. C40 showed the rapidest weight loss ratio and their weight loss reached 66.1 wt%, after soaking for 84 days. For comparison, the weight loss values of C20 and C0 were 38.1 and 15.3% after soaking for 84 days, respectively. Fig. 4B shows the pH variation of Tris-HCl solution containing the scaffolds for different periods of time. The pH of the solution containing C0 remained constant in the first 14 days and then dropped to pH 6.83 at the end of day 84. However, the pH of the solution containing C20 and C40 sharply increased to 7.62 and 7.70 in the first 4 days, and then remarkably decreased to 7.31 and 7.39 after 21 days of immersion, respectively. The pH of the solution with C20 decreased slightly to 7.17 while the solution with C40 showed no obvious change after further immersion for 84 days.

### 3.3 Apatite formation on scaffolds in SBF solution

The SEM images of the surface morphology of scaffolds after soaking into SBF for 5 days are shown in Fig. 5. No apatite was observed on the surface of C0 scaffolds. However, needle-like apatite particles could be found on the surfaces of C20 and C40 scaffolds. In addition, the cauliflower-like apatites on the surface of C40 were more than on C20 scaffolds. The results indicated that the introduction of m-MS significantly enhanced the apatite-formation ability of scaffolds in SBF, showing good bioactivity.

Fig. 6A presents the EDS of C40 before and after immersion in SBF solution for 5 days. The P and Ca peaks could be observed after immersion in SBF, indicating the formation of apatites on C40. Furthermore, the Ca/P ratio was 1.69, close to 1.67 (the Ca/P ratio of hydroxyapatite), which confirmed that the cauliflower-like substances covering the C40 scaffolds were apatites.

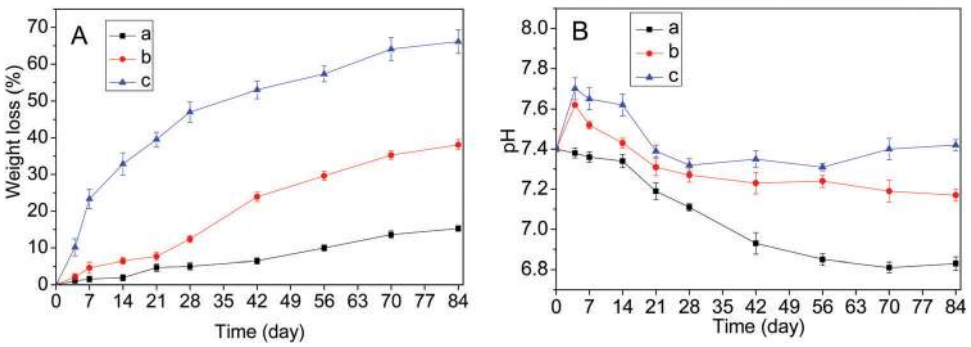


Fig. 4 Weight loss curves (A) and pH changes of solution (B) after soaking C0 (a), C20 (b), and C40 (c) scaffolds into Tris-HCl solution for different time periods.

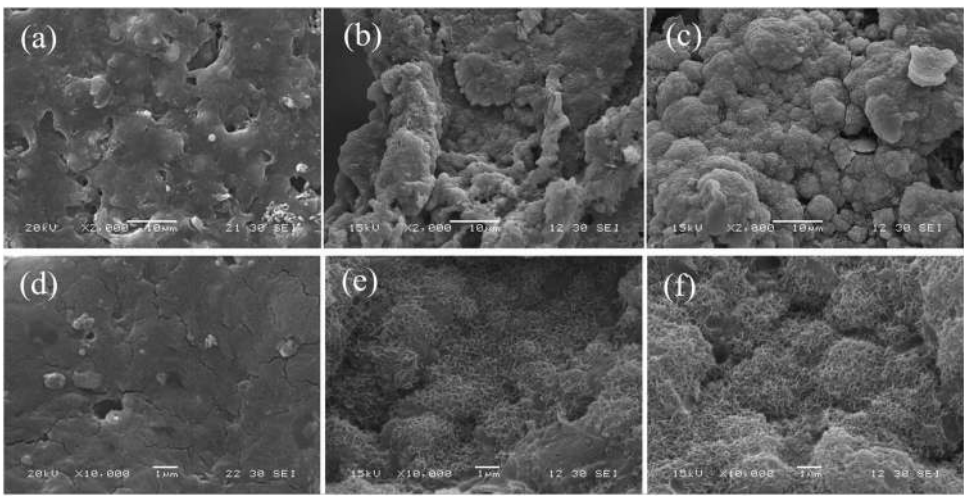


Fig. 5 SEM images of surface morphology of the C0 (a and d), C20 (b and e) and C40 (c and f) scaffolds after immersion into SBF for 5 days.

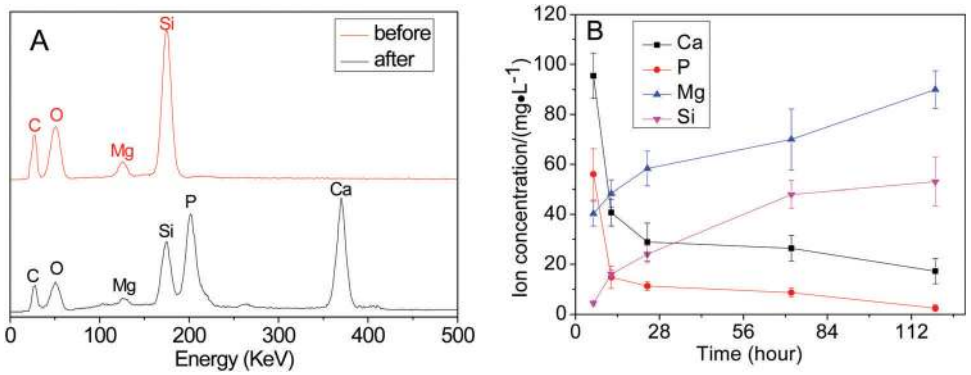


Fig. 6 EDS (A) of C40 scaffolds before and after immersion in SBF for 5 days and changes in the ion concentrations of SBF solution (B) after C40 immersion for different time periods.

### 3.4 Ionic concentration changes of SBF solution

Fig. 6B shows the changes in the ion concentration of SBF after C40 soaking for various time periods. The concentration of Ca and P ions in SBF solution decreased with immersion time, while the concentration of Mg and Si ions increased. This phenomenon could be due to the consumption of Ca and P ions during the formation of apatite. The increase in the concentration of Mg and Si ions was because of the degradation of C40 in SBF.

### 3.5 Cell viability

The viability of MC3T3-E1 cells was evaluated by the CCK-8 assay after the cells were seeded on the scaffolds for 3, 6, and 12 hours. As shown in Fig. 7d the modified ODs of C20 and C40 were significantly higher than C0 at 6 and 12 hours, indicating that more cells were on the C20 and C40 scaffolds than on C0 scaffolds. Furthermore, the modified OD of C40 was remarkably higher than C20 and C0 after culturing for 24 hours. These results suggested that more cells attached on C40 scaffolds than on C20 and C0 scaffolds.

Fig. 7 depicts the CLSM images of MC3T3-E1 cells showing their viability after being seeded on the scaffolds for 12 hours. Live MC3T3-E1 cells were stained green while the dead ones were stained red. It is found that some red dots were observed on the C0 and C20 scaffolds, indicating the presence of a few dead cells on the scaffolds. In addition, the green dots on C0 were found to gather together while the green dots on C20 were well dispersed, indicating that the live cells on C20 seemed to be more disperse than on C0 scaffolds. However, no red dots were found on C40, revealing no dead cells on the C40 scaffolds. Moreover, the number of green dots on C40 was more than those on C0 and C20, suggesting more live cells on C40 than the C20 and C0 scaffolds.

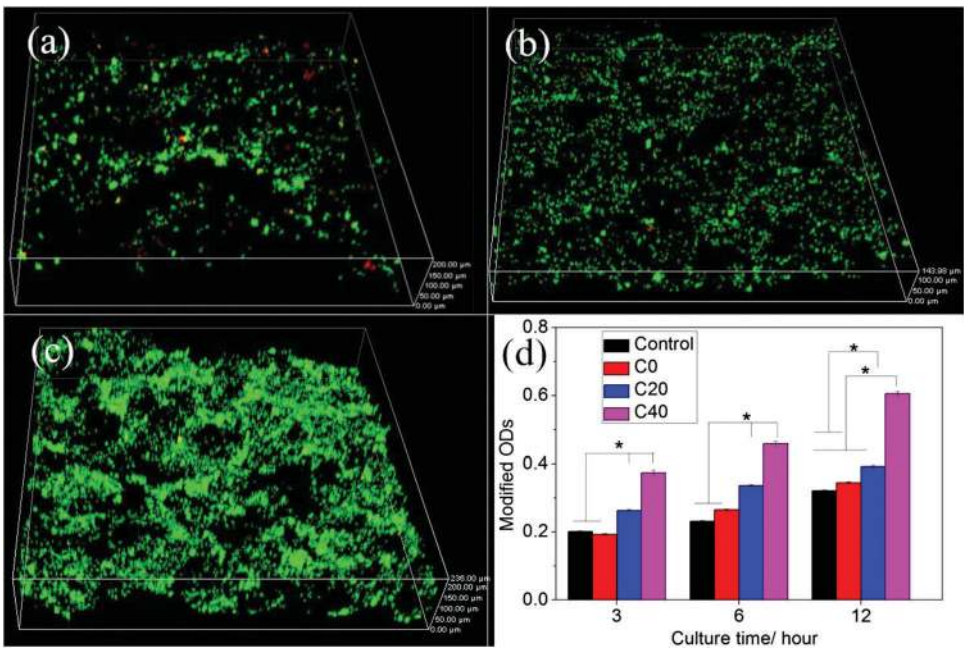


Fig. 7 CLSM images of MC3T3-E1 cells cultured on C0 (a), C20 (b) and C40 (c) scaffolds at 12 hours, showing live cells (green) and dead cells (red), and (d) cell attachment on scaffold surfaces by the CCK-8 assay.

 

### 3.6 Cell morphology and proliferation

Fig. 8 shows the CLSM images of MC3T3-E1 cells stained by FITC and DAPI on scaffolds, which displayed limpid F-actin after incubation for 3 days. The results revealed that the formation of an actin cytoskeleton on C0 distributed irregularly and in short fiber concentration, whereas the cells spreading on the C20 and C40 surfaces exhibited a typical fibroblastic morphology with more cytoplasmic extensions and filopodial attachments. It can be found that the cells grew into the macropores of the scaffolds. The ingrowth depths of cells along the macropores of C0, C20 and C40 scaffolds were 60, 100 and 140 μm, respectively.

Fig. 8d shows the proliferation of cells cultured on scaffolds. The relative proliferation ratios of cells on all scaffolds were increased over culture time. At day 3, the relative proliferation rate of cells on C0 was much lower than on C40 ($P < 0.05$), while no obvious difference was found between C40 and C20. In addition, the relative proliferation ratio of cells on C0 was significantly lower than on C40 ($P < 0.01$) and C20 ($P < 0.05$) at day 5.

### 3.7 Alkaline phosphatase activity

The ALP activity of MC3T3-E1 cells on scaffolds at day 7, 10 and 14 is shown in Fig. 9. It can be observed that the ALP activity of cells on all the scaffolds increased over culture time. Notably, the ALP activity of cells on the C40 showed significantly higher values than both C20 and C0 scaffolds at day 7 and 10 ($P < 0.05$). Furthermore, the ALP activity of cells on both the C40 and C20 was obviously higher than C0 at day 14 ($P < 0.05$).

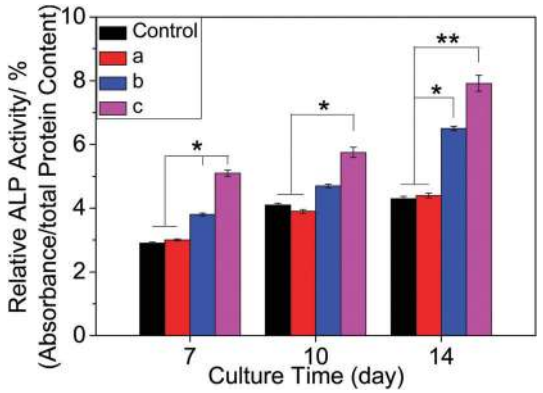


Fig. 9 ALP activity of MC3T3-E1 cells on C0 (a), C20 (b) and C40(c) scaffolds at 7, 10 and 14 days, and TCP as a control.

### 3.8 Ion concentration of cell culture medium

The ion concentrations of Si and Mg in the collected cell culture medium were determined. The results showed that the concentrations of Si and Mg ions for C0 stabilized at around 0.4 mg $L^{-1}$

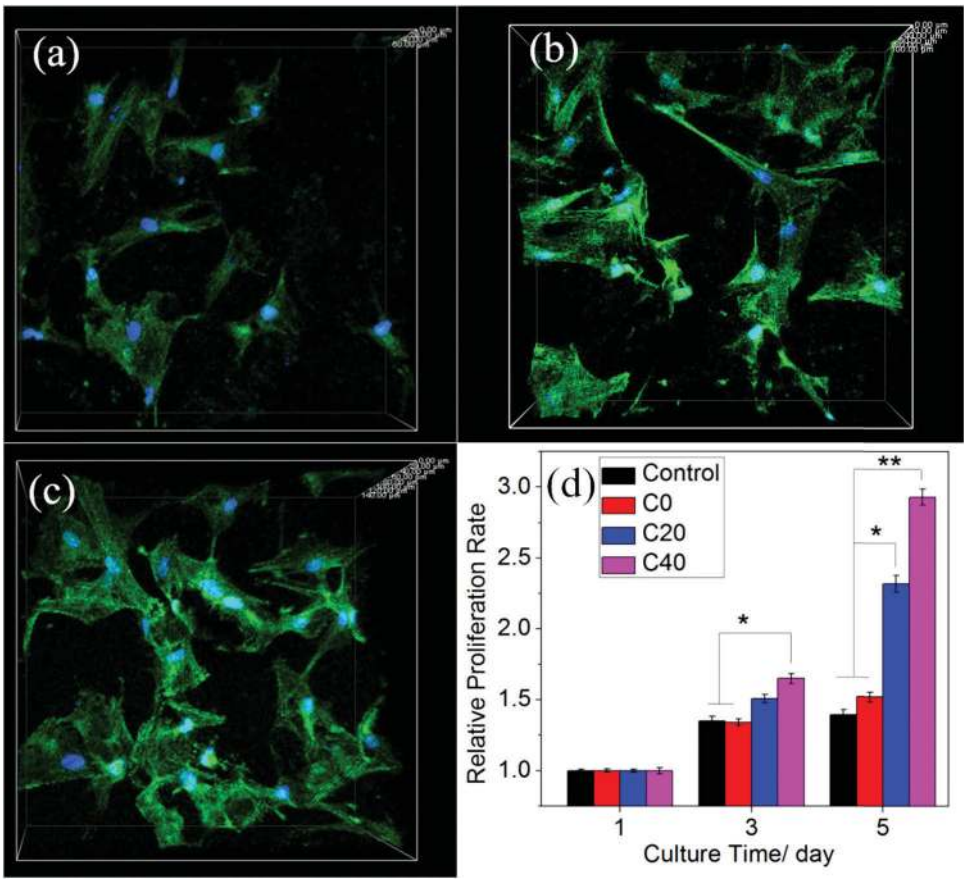


Fig. 8 CLSM of the cytoskeleton stained by FITC and DAPI at 3 days: C0 (a), C20 (b) and C40 (c) scaffolds, and (d) cell proliferation on the scaffold surfaces by the CCK-8 assay.

and 13 mg $L^{-1}$, which were similar to the control group. The concentrations of Mg and Si ions in cell culture medium for C20 and C40 were much higher than for C0 and the control. The concentration of Mg ions for C40 significantly increased during the first 5 days, and then stabilized approximately at 75 mg $L^{-1}$. However, there was no obvious change in the concentration of Si for C40 (around 28 mg $L^{-1}$) during the duration of cell culture. Furthermore, the ion concentrations of both Si and Mg for C40 were significantly higher than for C20 at any time point. The result thus indicated that the composite scaffolds containing m-MS released Mg and Si ions into the cell culture medium.

### 3.9 Implantation *in vivo*

**3.9.1 SRmCT analysis.** The quantity of bone regeneration stimulated by the scaffolds in rabbit femur cavity defects was evaluated by SRmCT (Fig. 10). At week 4, the SRmCT images revealed that obvious bone formation in the defects implanted with the C40 scaffold. Conversely, only a small amount of new bone formed in the defects for C0 and C20 scaffolds. 8 weeks after implantation, the amount of newly formed bone in all groups slightly increased. SRmCT examination showed the obvious bone ingrowth inside the C20 and C40 scaffolds, and the newly formed bone in the defects for the C40 scaffold seemed to possess higher density than C20. For comparison, there was no evidence of mineralized tissues in the defects for C0. At 12 weeks post-operation, C40 significantly induced more new bone tissues than C20 and C0, and the defects for C40 were completely repaired. However, the least amount of new bone was found in defects for C0, and the defects were not repaired.

**3.9.2 Histological analysis.** Fig. 11A shows the photomicrographs of histological sections (H&E staining), revealing more detailed information on new bone formation induced by scaffolds after implantation for 4, 8 and 12 weeks, respectively. The new bone tissue was found to increase gradually while all the scaffolds degraded accordingly over implantation time. In addition, the new bone tissue increased with the increase of the m-MS content in the scaffolds (C40 > C20 > C0) with the same implantation period. Furthermore, at 12 weeks after implantation, a large number of red bone marrows were observed to be surrounded by new bone composed of the mature meshwork of bone trabeculae, suggesting the formation of a medullary cavity in C40. Fig. 11B shows the quantity of new bone area for three kinds of scaffolds calculated from the corresponding histological images. It is found that the new bone area progressively increased over time for all the scaffolds while the new bone area for C40 was obviously higher than both C20 and C0 at week 12.

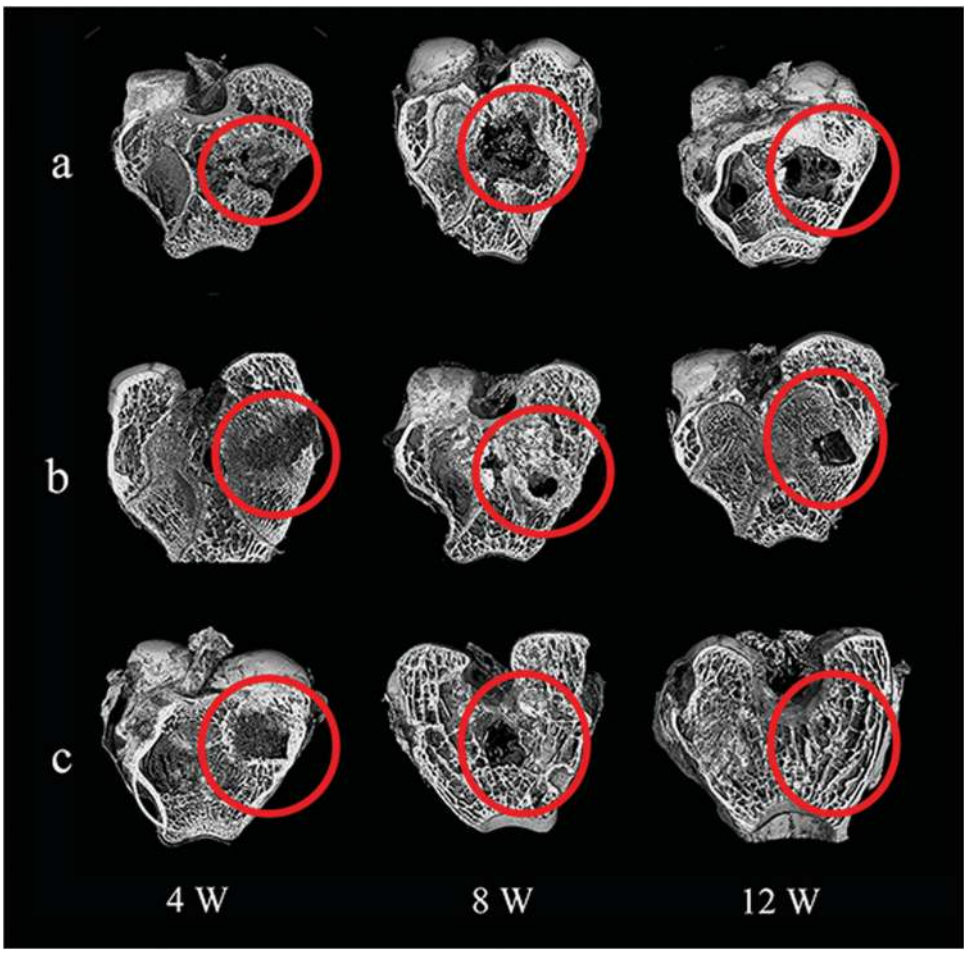


Fig. 10 Tridimensional reconstruction images by SRmCT of C0 (a), C20 (b) and C40 (c) scaffolds implanted in the bone defects of rabbit femur.

 

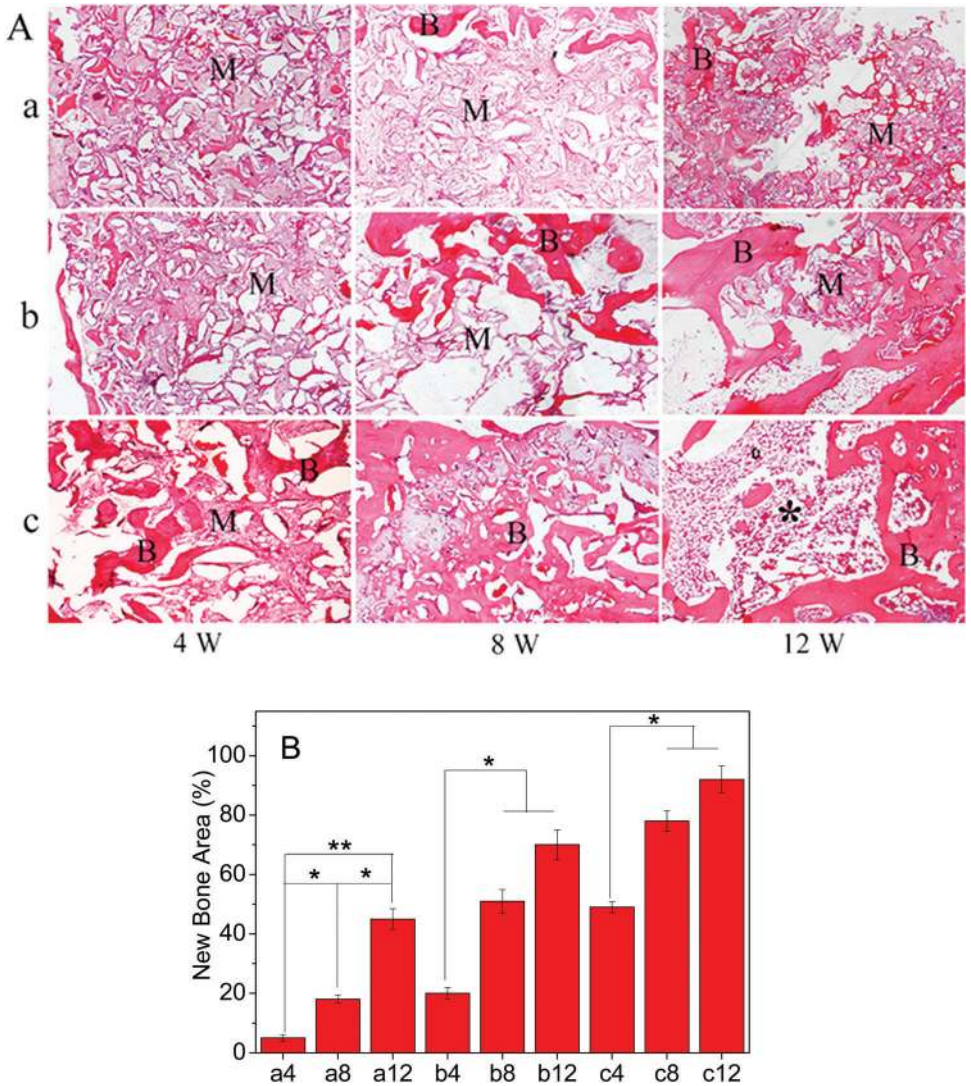


Fig. 11 (A) Histological evaluation (H&E staining) of new bone formation after C0 (a), C20 (b) and C40 (c) scaffolds implanted *in vivo* at 4, 8 and 12 weeks, respectively (100× magnification; M: material; B: new bone; *: bone marrow). (B) Quantitative analysis of the new bone area by histological observation.

Fig. 12A shows the photomicrographs of histological sections (Masson trichrome staining) in the defect sites after implantation of C0, C20 and C40 for 4, 8 and 12 weeks. Masson trichrome staining of histological sections can provide supplementary information on H&E staining, suggesting materials resorption and mature bone formation. The maturation of the new bone was a gradual process that involved dynamic interactions between implants and invaded bone cells/tissues. It is found that all the scaffolds degraded continually and new bone became matured over time. The largest quantity of mature bone formed in the defect containing C40 while least mature bone formed in the defect with C0 for the same implantation time, which is shown in both the microscopic images and quantitative analysis (Fig. 12A and B).

**3.9.3 Immunohistochemistry.** Fig. 13A shows the immunohistological analysis of BMP-2 on C0, C20 and C40 scaffolds after 4, 8 and 12 weeks of implantation, respectively. Brown staining in histological sections indicated the positive expression of BMP-2 in the new bone matrix. It is found that the positive expression area of BMP-2 for all three scaffolds increased over time, and it also increased with the m-MS content in the scaffolds (C40 > C20 > C0).

Fig. 13B shows the quantitative analysis of the positive expression ratio of BMP-2 on the scaffolds, which was calculated according to the microscopic images. It can be observed that the BMP-2-positive expression ratios of both the C40 and C20 were significantly higher than C0 scaffolds at week 4. No obvious difference was found for all the scaffolds at week 8. However, it is found that the BMP-2-positive expression ratio of C40 was remarkably higher than C20 and C0 scaffolds after 12 weeks of implantation.

## 4. Discussion

In the bone tissue engineering strategy, the scaffolds are of crucial importance since they act as porous temporary templates

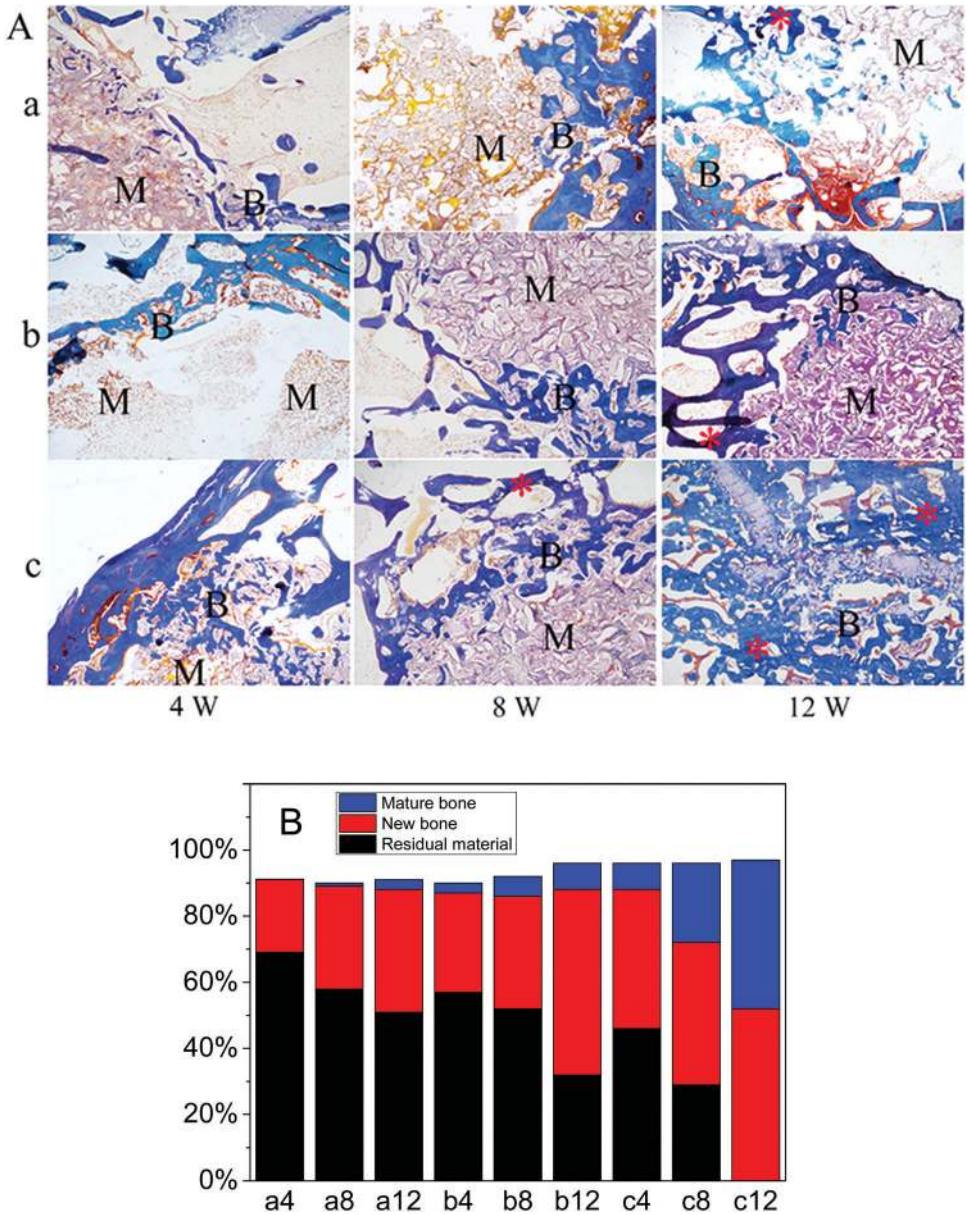


Fig. 12 (A) Histological evaluation (Masson trichrome staining) after C0 (a), C20 (b) and C40 (c) scaffold implantation *in vivo* for 4, 8 and 12 weeks, respectively (100× magnification; M: material; B: new bone; *: mature bone). (B) Quantitative analysis of new bone formation by histological observation.

for cell adhesion, proliferation, ensuing osteogenic differentiation and ultimately the regeneration of new bone tissue in three dimensions.[23] It is believed that one of the fundamental requirements for bone implanted scaffolds is an appropriate pore structure, such as high porosity and pore size (>300 μm),[24] which is essential for the ingrowth of cells and new bone tissue. In this study, the hierarchical porous architecture of scaffolds was characterized by both SRmCT and SEM. The m-MS/PBSu composite scaffold (C40) exhibited a highly porous structure with a porosity around 70%. The composite scaffold presented macropores with pore morphology and size (300–500 μm) similar to the geometry of salt particles, indicating that the macropores were induced by the leaching of salt. The formation of micropores ranging from 1 to 10 μm on the scaffold surfaces could be a result of solvent extraction.

Additionally, the introduction of m-MS possessing the uniform mesoporous channels of 8 nm led to the mesoporous structure of the scaffolds. The scaffold surface became rougher after the introduction of m-MS and the particles inlaid on the walls of the macropores, with the increase of m-MS content. The existence of micropores could result in an increase in the porosity of scaffolds, while the mesopores could cause the escalation of specific surface area. Another important role of micropores and mesopores is the possibility of loading with drugs or biomolecules to act as a controlled drug release system. In conclusion, the m-MS/PBSu composite scaffolds with a hierarchically macro–micro-mesoporous structure could be fabricated by a convenient salt-leaching method and this unique porous structure could be favourable for host cell

 

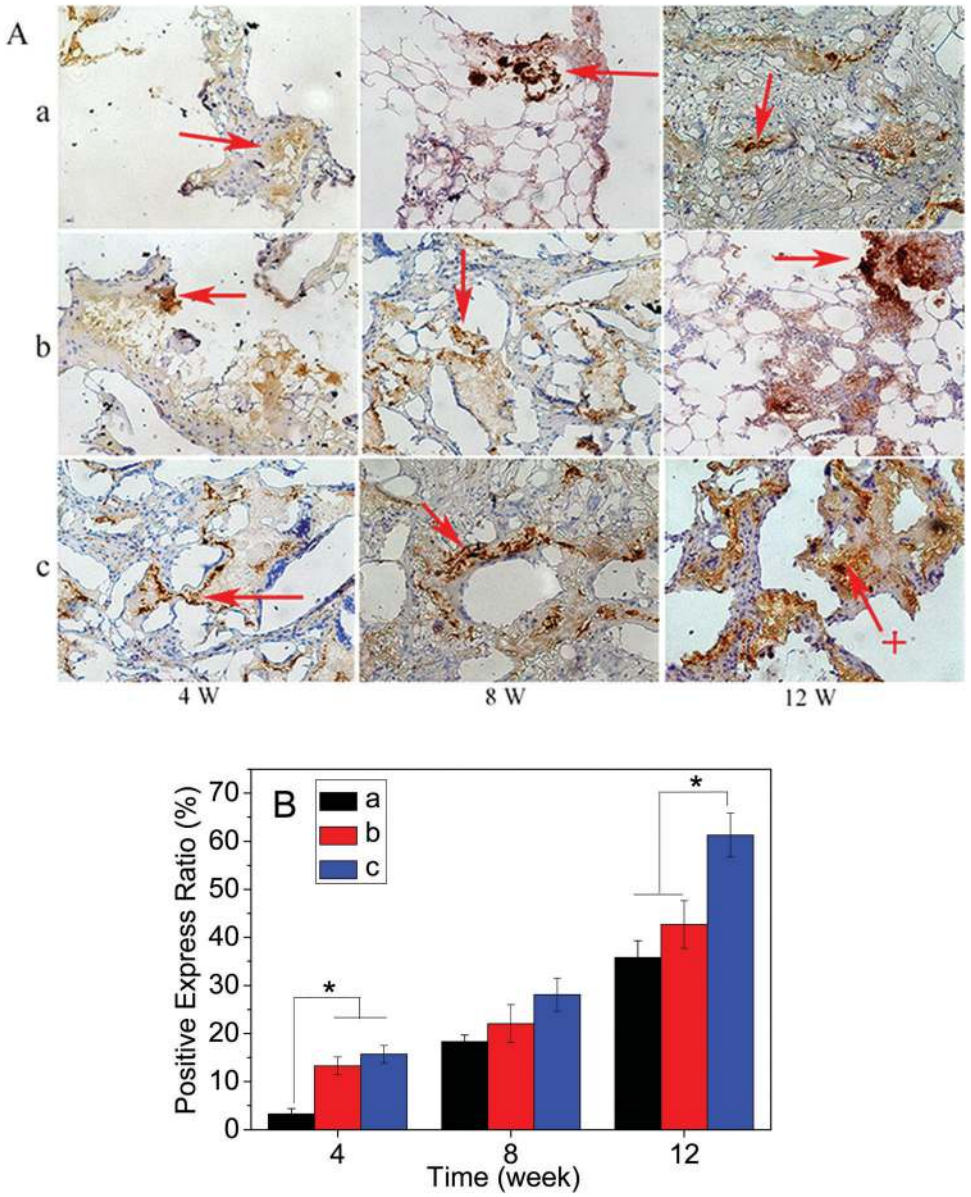


Fig. 13 (A) Immunohistological analysis of BMP-2 after C0 (a), C20 (b) and C40 (c) scaffold implantation *in vivo* for 4, 8 and 12 weeks, respectively. Brown staining indicates positive expression of BMP-2 (100× magnification). (B) Quantitative analysis of the positive expression ratio by histological observation.

migration with efficient exchange of nutrients throughout 3D spaces *in vivo*.

Besides pore size, pore interconnectivity also plays a vital role in promoting the ingrowth of cells/tissue into scaffolds.[25] In this study, it can be seen from the SRmCT images (Fig. 2) that the scaffolds with well interconnected macropores were 3D sponge-like porous structures. From SEM images (Fig. 3), it can be seen that the regularity of macropores decreased while the roughness and the number of micropores on macroporous walls increased, with the m-MS content. The results indicated that the scaffolds had good interconnectivity, which were beneficial to the flow transport of nutrients and wastes.

It is known that hydrophilicity is an important characteristic being favourable for cell attachment and spreading.[26] As an indicator of hydrophilicity, water absorption has been discussed in several studies.[27,28] In the present study, the results showed that all the scaffolds could absorb water in abundance, due to the masses of macropores and high porosity. However, the water absorption ratio of C40 (370%) was approximately 2-fold higher than that of C0 (190%) during the first half an hour of soaking, because of the larger specific surface area and capillarity caused by the mesopores in the scaffolds. Additionally, the presence of m-MS may also improve the water adsorption.[12] The water absorption increased from approximately 380% (C20) to more than 420% (C40), which could be due to the higher m-MS content in C40. With the highest water absorption ratio, C40 scaffolds were expected to be able to absorb the largest amount of body fluid after implantation *in vivo*, which could be conducive to the transfer of nutrients and metabolites of cells.

In the design of scaffolds for bone tissue engineering, appropriate degradability is an important factor that must be taken into account.[29] In this study, it is found that the weight loss of all the scaffolds increased as a function of soaking time. In addition, the weight loss ratio increased with the increase of m-MS content in composite scaffolds. Therefore, addition of m-MS to PBSu improved the degradability of the scaffolds. The incorporation of m-MS into the scaffolds could disturb the structure of PBSu, thereby resulting in the decrease of crystallinity. On the other hand, the degradation of m-MS on the walls of macropores could create more micropores on the walls, which could assist in the diffusion of medium into the interior of the scaffolds. This diffusion could thus further facilitate the hydrolytic degradation of PBSu. In addition, the weight loss of scaffolds increased with the increase of m-MS content, which was due to the relatively rapid degradation rate of m-MS. Thus, the degradation rate of scaffolds could be regulated by conveniently adjusting the m-MS content in the composite to match the regeneration rate of new bone tissue *in vivo*.

As we know, the main degradation product of PBSu is succinic acid, which causes the continuous decrease of the pH value of Tris-HCl solution containing C0. However, with the addition of m-MS, the pH value for C20 and C40 increased initially and then decreased. In the first 4 days of immersion, the m-MS on the walls of macropores was firstly degraded and $Mg^{2+}$ and $SiO_4^{4-}$ were released, resulting in a weak alkaline environment. With the immersion time, the main degradable product of PBSu (succinic acid) gradually increased, so the pH decreased slightly. In other words, the degradation of the m-MS in C20 and C40 could neutralize the acidic degradable products from PBSu, and thus compensated for the decrease of pH, compared to C0.

It is well-acknowledged that the ability to induce apatite formation is the indication of *in vivo* bioactivity of implants.[30] In the present study, the bioactivity was verified by the incubation of scaffolds in SBF solution, which is one of the methods for predicting the bone-forming ability.[31] The results showed that the apatite could definitely form on the surface of m-MS/PBSu composite scaffolds (both C20 and C40), while no apatite deposition was observed on PBSu scaffolds in the same immersion time. This indicated that addition of m-MS to bioinert PBSu could improve the bioactivity of composite scaffolds. In addition, more apatite formed on C40 than on C20 scaffolds, suggesting that the bioactivity of scaffolds could enhance with the increase of m-MS content. The decrease of Ca and P ion concentrations in SBF during the immersion of C40 indicated the formation of apatites. At the same time, the release of Si and Mg ions from C40 might accelerate apatite deposition, due to the presence of Si–OH groups that act as a catalyzing agent and the positive effect of $Mg^{2+}$ on the early stage of mineralization.[32] The results indicated that C40 scaffolds possessed *in vitro* bioactivity with apatite formation on the scaffold surfaces, which could improve the biological responses, such as cell proliferation and differentiation, *etc.* Previous studies have shown that the formation of apatite on the surfaces of bioactive materials could improve cell attachment and proliferation.[33] In this study, apatite could form on the m-MS/PBSu composite scaffold surfaces, which might promote cell attachment and proliferation.

The interaction of the cells with a biomaterial surface is considered to be a vital step in the evaluation of the biomaterial.[34,35] In this study, the interactions between MC3T3-E1 cells and the m-MS/PBSu composite scaffolds in 3D environments were studied, and the cell viability on the scaffolds was evaluated using the CCK-8 assay and the live/dead kit. The results showed that the number of live cells on C40 was the highest while that on C0 was the lowest. The cells on the m-MS/PBSu composite scaffolds spread better and extended with more pseudopods anchoring at the material surface, and connected with the neighboring cells, compared with PBSu scaffolds. It can be suggested that the existence of micropores and mesopores on the walls of the composite scaffolds was conducive to the pseudopod anchor of cells. Clearly, the osteoblasts preferred the rougher and more hydrophilic surface of the composite scaffolds rather than the smooth and hydrophobic surface of PBSu scaffolds. Therefore, the improved hydrophilicity, hierarchical porosity, release of Si and Mg ions, and roughness caused by the introduction of m-MS into PBSu scaffolds might contribute to the enhanced cell biological responses.

Moreover, the CCK-8 assay revealed that the m-MS/PBSu composite scaffolds could significantly stimulate cell proliferation compared with PBSu scaffolds after 5 days of culture. Si and Mg ions have been reported to promote proliferation and differentiation of osteoblasts, respectively.[36,37] Wu *et al.*[38] showed that the ion concentration of Si of $\sim$21.4 mg $L^{-1}$ in cell culture medium enhanced the proliferation of human bone marrow stromal cells. Gu *et al.*[39] reported that the extract with Si and Mg ions (ion concentrations of 40 mg $L^{-1}$ and 25 mg $L^{-1}$, respectively) from silicate elicited a stimulatory effect on the proliferation of human adipose-derived stem cells. In this study, it was found that the Si and Mg ions released from the m-MS/PBSu composite scaffolds into cell culture medium, and the ion concentrations of Si and Mg were 28 mg $L^{-1}$ and 78 mg $L^{-1}$ at 5 days, which were almost similar to the values previously reported. Therefore, it can be suggested that the Si and Mg ions with certain concentration released from the m-MS/PBSu composite scaffolds promoted the proliferation of MC3T3-E1 cells.

ALP activity, a marker for early osteoblast differentiation, is a critical factor for bone-implant interfacial osteointegration.[40] Xia *et al.*[41] found that the incorporation of Si ions into hydroxyapatite enhanced the osteogenic differentiation of rat bone marrow stromal cells (Si ion concentration of 70 mg $L^{-1}$ releasing from the materials). Fei *et al.*[42] showed that Si ions (ion concentration of 69.2 mg $L^{-1}$) released from calcium silicate/β-tricalcium phosphate increased the ALP activity and gene expression of osteocalcin. Zhang *et al.*[43] showed that Mg ions (ion concentration of 85.2 mg $L^{-1}$) released from akermanite enhanced the ALP activity of human bone marrow stromal cells. Wu *et al.*[44] has shown that the Mg ions (ion concentration of 76 mg $L^{-1}$) promoted the osteogenic differentiation of human bone marrow stromal cells. In this study the results suggested that the ion concentrations of Si and Mg in the cell culture medium for C40 were 27 mg $L^{-1}$ and 72 mg $L^{-1}$ at 14 days, which were significantly higher than for C20 and C0. Moreover, the ALP activity of cells for C40 was significantly higher than

 

that for C20 and C0 scaffolds. This result indicates that Mg and Si ions released in a given concentration from C40 could improve the ALP activity of MC3T3-E1 cells. Therefore, it can be stated that m-MS/PBSu composite scaffolds promoted osteogenic differentiation by the release of Mg and Si ions into culture medium.

The *in vivo* bone regeneration potential of m-MS/PBSu composite scaffolds was evaluated by implanting the scaffolds into the radius defects of rabbits. The SRmCT and histological analysis results revealed that the composite scaffolds degraded and were replaced by new bone tissue over time. Compared with the C20 scaffolds, the C40 scaffolds induced more new bone formation. Furthermore, red bone marrow and more mature bone could be observed on defects implanted with C40. Additionally, it was noted that the BMP-2-positive expression ratio for C40 was the highest among the scaffolds. The strong osteogenic outcomes induced by m-MS/PBSu composite scaffolds could be attributed to the incorporation of m-MS, which released Mg and Si ions to promote bone regeneration *in vivo*.

Specifically, Si ions were reported to effectively enhance the gene expression related to bone matrix synthesis and osteoblastic activity (forming mineralization nodules), as well as to stimulate bone matrix protein (COL-I) synthesis;[45] Mg ions, one of the most important mineral elements in the bone matrix, were found to regulate active calcium transport, stabilize the structure of DNA, and even influence all stages of skeletal metabolism.[46,47] Given the functions of Si and Mg ions, the incorporation of m-MS into PBSu scaffolds could lead to the release of biologically active ions at the defects, which could control the local pH in a suitable range for cell viability, and stimulate the new bone regeneration. As seen in the histological images, the implantation of m-MS/PBSu composite scaffolds did not cause any adverse reactions during the whole periods, indicating good biocompatibility. These results confirmed that the incorporation of m-MS into PBSu and composite scaffolds with a hierarchically macro–micro-mesoporous structure significantly promoted the biological responses, such as cell attachment, proliferation, differentiation and bone regeneration.

## 5. Conclusions

In this study, degradable and bioactive scaffolds of m-MS/PBSu composites with a hierarchically macro–micro-mesoporous structure were fabricated for bone repair. The incorporation of m-MS into PBSu enhanced the compressive strength, hydrophilicity, degradability and bioactivity of composite scaffolds. In addition, the composite scaffolds improved the *in vitro* attachment, proliferation and differentiation of MC3T3-E1 cells, revealing good cytocompatibility. According to the SRmCT, histological and immunohistochemical evaluation, the results revealed that the C40 scaffolds containing m-MS significantly promoted degradability and osteogenesis *in vivo*. Our studies demonstrated that the incorporation of m-MS into PBSu apparently improved the biological responses, including cell proliferation, differentiation and bone regeneration both *in vitro* and *in vivo*. The improvement of the biological responses might be attributed to the Mg and Si ions released from composite scaffolds. In short, the m-MS/PBSu composite scaffolds with good biocompatibility, biodegradability and osteogenesis are promising candidates for bone repair applications.

## Acknowledgements

The grants were from the National key research and development program (2016YFC1102100), the National Natural Science Foundation of China (81271705, 31271031), the Major International Joint Research Project between China and Korea (81461148033), the National Research Foundation of Korea (NRF) Grant (NRF-2014K2A2A7066637), the China Scholarship Council (CSC)-German Academic Exchange Service (DAAD) PPP project and CSC (No. 201206740003).

## References

1 P. Bajaj, R. M. Schweller, A. Khademhosseini, J. L. West and R. Bashir, *Annu. Rev. Biomed. Eng.*, 2014, **16**, 247–276.
2 S. Farah, D. G. Anderson and R. Langer, *Adv. Drug Delivery Rev.*, 2016, DOI: 10.1016/j.addr.2016.06.012.
3 N. Du, W. Guo, Q. Yu, S. Guan, L. Guo, T. Shen, H. Tang and Z. Gan, *Polym. Chem.*, 2016, **7**, 5719–5729.
4 M. Naffakh and A. M. Díez-Pascual, *RSC Adv.*, 2015, **5**, 65514–65525.
5 L. Wei, N. M. Stark and A. G. McDonald, *Green Chem.*, 2015, **17**, 4800–4814.
6 N. Roy, B. Bruchmann and J. M. Lehn, *Chem. Soc. Rev.*, 2015, **44**, 3786–3807.
7 Q. Shi, X. Xu, Q. Fan, J. Hou, W. Ye and J. Yin, *J. Mater. Chem. B*, 2015, **3**, 2119–2126.
8 S. Wu, L. Zheng, C. Li, S. Huo, Y. Xiao, G. Guan and W. Zhu, *Polym. Chem.*, 2015, **6**, 1495–1501.
9 V. Ojijo, S. S. Ray and R. Sadiku, *ACS Appl. Mater. Interfaces*, 2013, **5**, 4266–4276.
10 A. M. Diez-Pascual and A. L. Diez-Vicente, *J. Mater. Chem. B*, 2016, **4**, 600–612.
11 S. Kango, S. Kalia, A. Celli, J. Njuguna, Y. Habibi and R. Kumar, *Prog. Polym. Sci.*, 2013, **38**, 1232–1261.
12 Z. Wu, T. Tang, H. Guo, S. Tang, Y. Niu, J. Zhang, W. Zhang, R. Ma, J. Su, C. Liu and J. Wei, *Colloids Surf., B*, 2014, **120**, 38–46.
13 M. Diba, O. M. Goudouri, F. Tapia and A. R. Boccaccini, *Curr. Opin. Solid State Mater. Sci.*, 2014, **18**, 147–167.
14 J. Zhang, X. Ma, D. Lin, H. Shi, Y. Yuan, W. Tang, H. Zhou, H. Guo, J. Qian and C. Liu, *Biomaterials*, 2015, **53**, 251–264.
15 M. Diba, F. Tapia, A. R. Boccaccini and L. A. Strobel, *Int. J. Appl. Glass Sci.*, 2012, **3**, 221–253.
16 X. Jin, H. Yu, N. Kong, J. Chang, H. Li and J. Ye, *J. Mater. Chem. B*, 2015, **3**, 7787–7795.
17 X. Liu, M. N. Rahaman, G. E. Hilmas and B. S. Bal, *Acta Biomater.*, 2013, **9**, 7025–7034.
18 C. C. Ho, S. C. Huang, C. K. Wei and S. J. Ding, *J. Mater. Chem. B*, 2016, **4**, 505–512.

19 D. Gregurec, G. Wang, R. H. Pires, M. Kosutic, T. Lüdtke, M. Delcea and S. E. Moya, *J. Mater. Chem. B*, 2016, **4**, 1978–1986.
20 R. Ma, S. Tang, H. Tan, J. Qian, W. Lin, Y. Wang, C. Liu, J. Wei and T. Tang, *ACS Appl. Mater. Interfaces*, 2014, **6**, 12214–12225.
21 W. Tang, D. Lin, Y. Yu, H. Niu, H. Guo, Y. Yuan and C. Liu, *Acta Biomater.*, 2016, **32**, 309–323.
22 S. Deepthi, C. Viha, C. Thitirat, T. Furuike, H. Tamura and R. Jayakumar, *Polymers*, 2014, **6**, 2974–2984.
23 J. Karlsson, G. Sundell, M. Thuvander and M. Andersson, *Nano Lett.*, 2014, **14**, 4220–4223.
24 L. Xia, Z. Yin, L. Mao, X. Wang, J. Liu, X. Jiang, Z. Zhang, K. Lin, J. Chang and B. Fang, *Sci. Rep.*, 2016, **6**, 22005.
25 A. Leal-Egana, A. Diaz-Cuenca and A. R. Boccaccini, *Adv. Mater.*, 2013, **25**, 4049–4057.
26 M. Matsusaki, C. P. Case and M. Akashi, *Adv. Drug Delivery Rev.*, 2014, **74**, 95–103.
27 Z. Sun, G. Cui, H. Li, Y. Liu, Y. Tian and S. Yan, *J. Mater. Chem. B*, 2016, **4**, 5194–5216.
28 J. L. Whittaker, N. K. Dutta, A. Zannettino and N. R. Choudhury, *J. Mater. Chem. B*, 2016, **4**, 5519–5533.
29 A. Sugawara, K. Asaoka and S.-J. Ding, *J. Mater. Chem. B*, 2013, **1**, 1081–1089.
30 Y. Huang, M. Yao, X. Zheng, X. Liang, X. Su, Y. Zhang, A. Lu and L. Zhang, *Biomacromolecules*, 2015, **16**, 3499–3507.
31 C.-C. Ho, S.-C. Huang, C.-K. Wei and S.-J. Ding, *J. Mater. Chem. B*, 2016, **4**, 505–512.
32 H. L. Jang, G. B. Zheng, J. Park, H. D. Kim, H.-R. Baek, H. K. Lee, K. Lee, H. N. Han, C.-K. Lee, N. S. Hwang, J. H. Lee and K. T. Nam, *Adv. Healthcare Mater.*, 2016, **5**, 128–136.
33 C. Wu, Z. Chen, Q. Wu, D. Yi, T. Friis, X. Zheng, J. Chang, X. Jiang and Y. Xiao, *Biomaterials*, 2015, **71**, 35–47.
34 S. Font Tellado, E. R. Balmayor and M. Van Griensven, *Adv. Drug Delivery Rev.*, 2015, **94**, 126–140.
35 B. R. Coad, S. J. Lamont-Friedrich, L. Gwynne, M. Jasieniak, S. S. Griesser, A. Traven, A. Y. Peleg and H. J. Griesser, *J. Mater. Chem. B*, 2015, **3**, 8469–8476.
36 J. Melke, S. Midha, S. Ghosh, K. Ito and S. Hofmann, *Acta Biomater.*, 2016, **31**, 1–16.
37 X. Zhang, D. Zeng, N. Li, X. Jiang, C. Liu and Y. Li, *J. Mater. Chem. B*, 2016, **4**, 3916–3924.
38 C. Wu, P. Han, M. Xu, X. Zhang, Y. Zhou, G. Xue, J. Chang and Y. Xiao, *J. Mater. Chem. B*, 2013, **1**, 876–885.
39 H. Gu, F. Guo, X. Zhou, L. Gong, Y. Zhang, W. Zhai, L. Chen, L. Cen, S. Yin, J. Chang and L. Cui, *Biomaterials*, 2011, **32**, 7023–7033.
40 H. Zhu, D. Zhai, C. Lin, Y. Zhang, Z. Huan, J. Chang and C. Wu, *J. Mater. Chem. B*, 2016, **4**, 6200–6212.
41 L. Xia, N. Zhang, X. Wang, Y. Zhou, L. Mao, J. Liu, X. Jiang, Z. Zhang, J. Chang, K. Lin and B. Fang, *J. Mater. Chem. B*, 2016, **4**, 3313–3323.
42 L. Fei, C. Wang, Y. Xue, K. Lin, J. Chang and J. Sun, *J. Biomed. Mater. Res., Part B*, 2012, **100**, 1237–1244.
43 M. Zhang, C. Wu, K. Lin, W. Fan, L. Chen, Y. Xiao and J. Chang, *J. Biomed. Mater. Res., Part A*, 2012, **100**, 2979–2990.
44 C. Wu, Z. Chen, D. Yi, J. Chang and Y. Xiao, *ACS Appl. Mater. Interfaces*, 2014, **6**, 4264–4276.
45 W. Li, H. Wang, Y. Ding, E. C. Scheithauer, O.-M. Goudouri, A. Grunewald, R. Detsch, S. Agarwal and A. R. Boccaccini, *J. Mater. Chem. B*, 2015, **3**, 3367–3378.
46 S. Bose, G. Fielding, S. Tarafder and A. Bandyopadhyay, *Trends Biotechnol.*, 2013, **31**, 594–605.
47 E. V. Skorb and D. V. Andreeva, *Adv. Funct. Mater.*, 2013, **23**, 4483–4506.

 